Surface & Coatings Technology 418 (2021) 127237

Contents lists available at ScienceDirect

Surface & Coatings Technology

journal homepage: www.elsevier.com/locate/surfcoat

Evolution of the microstructure of sputter deposited TaAlON thin films with increasing oxygen partial pressure

Nina Schalk [a,b,*], Christian Saringer [b], Alexander Fian [c], Velislava L. Terziyska [a], Jaakko Julin [d,e], Michael Tkadletz [a]

[a] Department of Materials Science, Montanuniversität Leoben, Franz-Josef-Straße 18, 8700 Leoben, Austria
[b] Christian Doppler Laboratory of Advanced Coated Cutting Tools, Department of Materials Science, Montanuniversität Leoben, Franz-Josef-Straße 18, 8700 Leoben, Austria
[c] Institute for Surface Technologies and Photonics, JOANNEUM RESEARCH Forschungsgesellschaft, Franz-Pichler-Straße 30, 8160 Weiz, Austria
[d] Institute of Ion Beam Physics and Materials Research, Helmholtz-Zentrum Dresden-Rossendorf, Bautzner Landstraße 400, 01328 Dresden, Germany
[e] Department of Physics, University of Jyväskylä, P.O. Box 35, 40014 University of Jyväskylä, Finland

ARTICLE INFO

Keywords:
Oxynitrides
TaAlON
Microstructure
TEM
XPS

ABSTRACT

Recently, quaternary oxynitrides of transition metals and aluminum have attracted increasing interest due to their tunable properties. Within the present work, a series of TaAl(*O*)N films was sputter deposited using constant nitrogen and varying oxygen partial pressures. The films were grown from single element Ta and Al targets. The deposition parameters were adjusted to obtain a Ta/Al atomic ratio of ~50/50 for the oxygen-free film and were held constant for the following depositions, with the exception of the increasing oxygen partial pressure and compensatory decreasing argon partial pressure. Elastic recoil detection analysis revealed oxygen contents of up to ~26 at.%, while the nitrogen content decreased from ~47 at.% in the oxygen-free film to ~35 at.% in the film with the highest oxygen content, resulting in a significant decrease of the metal/non-metal ratio with increasing oxygen partial pressure. The micro- and bonding structures of the films were investigated by X-ray diffraction, X-ray photoelectron spectroscopy, Raman spectroscopy and transmission electron microscopy. All films exhibited a dominating face-centered cubic TaN-based structure with indications for additional nanocrystalline and amorphous phase fractions in the oxygen containing films. In addition, the mechanical properties were evaluated by nanoindentation, yielding a decreasing hardness and elastic modulus with increasing oxygen content.

1. Introduction

In recent years, quaternary oxynitrides of transition metals (TM) and aluminum have attracted increasing interest due to the tunability of their properties by adjusting the O/N ratio [1–6]. The majority of the existing publications focuses on TiAlON and CrAlON thin films [1–14]. Only a few reports are available on alternative systems such as ZrAlON or HfAlON [15,16], while no literature can be found on TaAlON thin films. The enthalpies of formation for TiO_2 (−939 kJ/mol), Cr_2O_3 (−1140 kJ/mol) and ZrO_2 (−1097 kJ/mol) are less negative compared to Al_2O_3 (−1676 kJ/mol), while for Ta_2O_5 the enthalpy of formation is more negative (−2046 kJ/mol) [17]. For AlN, TiN and ZrN the enthalpies of formation are comparable with −318, −338 and −365 kJ/mol, respectively, while those for TaN and CrN are with −251 and −117 kJ/mol, respectively, even less negative [17,18]. Considering these values, it seems likely that the formation of oxides is governed by thermal activation provided during film growth, while for nitrides additional kinetic activation is necessary, which indicates that the phase formation depends on the involved elements and that compositional variations are present in oxynitrides [1,9,13,19]. Taking into account the different enthalpies of formation for the respective oxides of Ta and the other TMs mentioned above which have already been used for the deposition of TMAlON discussed in literature, a study of the microstructure and in particular the phase evolution of TaAlON thin films with increasing O content could significantly contribute to the further establishment of a fundamental understanding of the phase formation depending on the involved TM in oxynitrides.

Thus within the present work, a series of four TaAl(*O*)N thin films was sputter deposited applying different O_2 partial pressures. The elemental composition was determined using elastic recoil detection

* Corresponding author at: Department of Materials Science, Montanuniversität Leoben, Franz-Josef-Straße 18, 8700 Leoben, Austria.
E-mail address: nina.schalk@unileoben.ac.at (N. Schalk).

https://doi.org/10.1016/j.surfcoat.2021.127237
Received 2 March 2021; Received in revised form 22 April 2021; Accepted 23 April 2021
Available online 29 April 2021

analysis. The phase compositions and microstructures were investigated in detail utilizing a combinatorial approach of X-ray diffraction, X-ray photoelectron and Raman spectroscopy as well as transmission electron microscopy including selected area electron diffraction. In addition, the hardness and elastic modulus of the films was determined using nanoindentation.

2. Experimental details

Four TaAl(*O*)N films were synthesized on Si substrates using a lab-scale unbalanced d.c. magnetron sputter deposition system, equipped with one Ta (purity 99.95%) and one Al (purity 99.99%) target (ø 2 in., powder metallurgically produced) focused to the center of the substrate holder. The deposition chamber was evacuated to a base pressure of ~2 × 10^{-3} Pa. Prior to deposition, an additional Ar^+ ion etching step was implemented to clean the substrates, applying a voltage of −500 V at a frequency of 50 kHz for 10 min. The depositions were performed in constant power mode, where the power for the Ta target was set to 138 W and for the Al target to 142 W. In addition, the Al target was pulsed with a frequency of 50 kHz and 0.5 μs reverse time. An asymmetrically bipolarily pulsed DC bias voltage of −105 V with a frequency of 50 kHz and a duty cycle of 40% was applied to the substrates. The substrate rotation was set to 50 rpm, the target to substrate distance to 45 mm, the substrate temperature to 550 °C and the deposition time to 50 min. In order to obtain films with different O contents, the O_2 partial pressure p_{O2} was varied from 0 over 0.005 and 0.05 to 0.10 Pa, while the N_2 partial pressure was held constant at 0.3 Pa. The Ar partial pressure was adjusted to obtain a constant total pressure of ~0.80 Pa.

The film thicknesses were determined using the ball cratering technique. Elastic recoil detection analysis (ERDA) measurements were performed to determine elemental composition of the films, using a $^{35}Cl^{7+}$ ion beam with an energy of 43 MeV. The investigated area was ~2 × 2 mm^2, the angle between sample normal and beam 75° and the scattering angle 29.5°. A Bragg Ionization Chamber was used to detect the recoiling atoms and scattered Cl ions. For compositions below 10 at.%, a relative accuracy of ±1% of the measured value and for compositions above 10 at.% an absolute accuracy of ±1% can be assumed. The microstructure of the films was studied by X-ray diffraction (XRD), using a Bruker-AXS D8 Advance diffractometer in θ–2θ geometry. In addition, an Omicron Multiprobe surface analysis system equipped with a DAR 400 X-ray source, an XM 500 quartz crystal monochromator (X-ray excitation energy of 1486.7 eV, Al $K_{\alpha 1}$) and an EA 125 hemispherical electron energy analyzer with a 5-channel pulse counting channeltron was applied to investigate the chemical structure by X-ray photoelectron spectroscopy (XPS). The spectrometer was calibrated according to NIST-standard using Au, Ag and Cu samples [20]. At the applied pass energy of 20 eV, the overall energy resolution of the system is 0.5 eV (according to the calibration data). The binding energy axis was referenced to the C—C bond of the C1s peak at 284.6 eV of residual hydrocarbon surface contaminants, as determined on the calibration samples. A critical review of using this peak as a reference can be found in ref. [21]. We have, therefore, additionally checked the binding energy of the Ta4f7/2 peak of the Ta_2O_5 component in the Ta4f spectra (26.7 eV) and observed excellent agreement with literature values (26.6 eV) [22]. The base pressure of the vacuum chamber was around 10^{-10} mbar, the analyzed area 1 mm in diameter. Charge compensation by an electron flood gun was not necessary due to sufficient conductivity of the samples. The XPS measurements were performed in as-received state at three different detection angles (0, 35 and 50°) to the surface normal, in order to be able to distinguish surface layers/contaminants and constituents of the actual film. Attempts to remove surface contaminants by Ar-sputtering or annealing turned out to provoke chemical decomposition of the surface chemistry even at very low sputtering energies (500 eV), but also at annealing temperatures sufficiently high for the removal of adsorbed molecules (250 °C). The obtained spectra were fitted with the spectra processing software UNIFIT 2017 using a Voigt function [23] and a Shirley background [24]. Complementary, a Horiba Jobin-Yvon LABRAM confocal Raman spectrometer equipped with a frequency-doubled Nd-YAG laser (λ = 532.2 nm) was employed to obtain further information about the chemical structure. In addition, the film deposited at p_{O2} = 0.05 Pa was investigated in detail using an FEI Titan 3 G2 60–300 scanning transmission electron microscope (S/TEM) equipped with an X-FEG Schottky field emission electron gun operated at 300 kV. The current was 150 pA and the beam diameter 1 Å. A FEI Super-X detector (Chemi-STEM technology), consisting of four separate Si drift detectors, was applied to acquire spectrum images. Selected area electron diffraction (SAED) patterns of the same film were recorded utilizing a Tecnai 12 TEM, equipped with a LaB_6 cathode operated at 120 kV. The TEM lamella was prepared using a focused ion beam workstation combined with a field emission gun scanning electron microscope (FEI NOVA 200 NanoLab).

The hardness and elastic modulus of the films were determined using an UMIS (Ultra Micro Indentation System) nanoindenter from Fischer-Cripps Laboratories, equipped with a diamond Berkovich tip. A plateau test with a minimum load of 5 mN, increments of 1 mN and a maximum load of 30 mN was carried out. The maximum load was chosen to result in a maximum indentation depth of below 10% of the film thickness.

3. Results and discussion

The thicknesses of the TaAlN film deposited without the addition of O and the TaAlON film deposited at p_{O2} = 0.005 Pa are 1.8 and 1.9 μm, respectively and thus, comparable. The thicknesses of the films grown at higher p_{O2} of 0.05 and 0.10 Pa are with 1.4 and 1.5 μm, respectively, clearly thinner. Thus, there is no constant trend to lower thicknesses with increasing p_{O2}, but a drop in the deposition rate between p_{O2} = 0.005 and 0.05 Pa from 37 ± 1 to 29 ± 1 nm/min. The evolution of the elemental composition with increasing p_{O2} is shown in Fig. 1a. For the film deposited without the addition of O, below 1 at.% O was detected using ERDA, which can be attributed to residual O in the deposition chamber. The ERDA results suggest that the film is substoichiometric with respect to the N content (47 at.%) and the Al/(Al + Ta) ratio is 0.48. Adding p_{O2} = 0.005 Pa results in 10 at.% O, while the N content only marginally decreases to 45 at.%, entailing a distinct drop of the metal/non-metal ratio (Ta + Al)/(O + N) to 0.79 from 1.09 for the O-free film. A decreasing metal/non-metal ratio with increasing O content is typically also observed for TiAlON and CrAlON films, where the accompanying increasing presence of metal vacancies is also predicted by quantum mechanical calculations [1,8,9,12,25,26]. The Al/(Al + Ta) ratio decreases to 0.40. Further increasing of $p_{O2}$to 0.05 Pa causes again a significant increase of the O content to 23 at.% and a comparably moderate decrease of the N content to 37 at.%, resulting in a further decrease of the metal/non-metal ratio to 0.67. Also the Al/(Al + Ta) ratio further decreases to 0.32. The increase of the O content with further increasing $p_{O2}$to 0.10 Pa is not that pronounced anymore, resulting in a maximum O content of 26 at.% in this study, while the N content decreases only slightly to 35 at.%, entailing a minor decrease of the metal/non-metal ratio to 0.63. The Al/(Al + Ta) ratio further decreases significantly to 0.26. Considering the evolution of the elemental composition and the evolution of the deposition rate with increasing p_{O2}, it appears at first glance that poisoning of the Al target occurs at p_{O2} > 0.05 Pa [27–29]. Thus, it seems reasonable to take a closer look at the deposition characteristics. In Fig. 1b, the evolution of the target voltage with increasing p_{O2} is shown for both, the Al and the Ta target. The for target poisoning typical sudden change of the voltage cannot be observed for the Al target. The voltage of the Ta target does slightly increase, but not abruptly and as the Ta content in the films even slightly increases with increasing p_{O2} and the deposition rates are still reasonable, target poisoning seems not to play a role here. In order to illuminate contributions from different sputter behavior of the two different targets, the SRIM (Stopping and Range of Ions in Matter) code [30] was

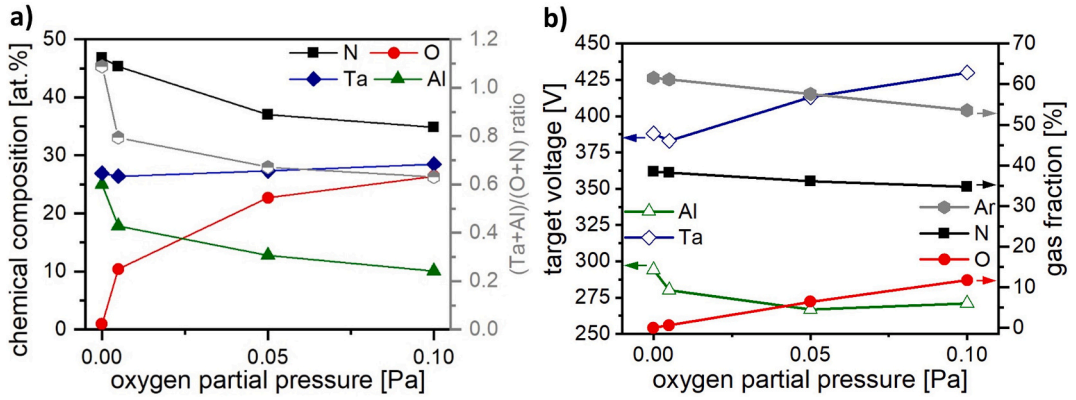

Fig. 1. Evolution of the (a) elemental composition determined by ERDA and (b) the target voltage and gas composition during the deposition process of the TaAl(*O*)N films as a function of the O_2 partial pressure p_{O2}.

applied to calculate the sputter yields and energy of ejected neutrals for the different gas compositions evolving as a result of increasing p_{O2} and considering the respective ion energies. For the ion energies, the target voltages summarized in Fig. 1b were used as approximation, neglecting the plasma potential. The evolution of the gas composition is also summarized in Fig. 1b. The total pressure slightly increased with increasing p_{O2} (from 0.80 Pa for the O-free film to 0.88 Pa for $p_{O2} = 0.1$ Pa), due to insufficient adjustment of the Ar partial pressure, resulting at constant N_2 partial pressure in a slightly decreasing nitrogen fraction in the process gas. The obtained sputter yield for both, the Al and the Ta target, is 0.64 ± 0.02 atoms/ion for all p_{O2}. The comparable values for Al and Ta are a result of the gas mixture with light reactive gas elements and heavier Ar and the different applied target voltages. However, the energy of neutrals leaving the target is with ~24 eV/atom significantly higher for Ta than for Al atoms, where ~12 eV/atom were determined using the SRIM code. These values represent the energy of the sputtered atoms leaving the target surface and do not consider energy losses due to scattering processes. During the transport phase from target to substrate, the atoms may lose energy and be scattered due to collision processes, which is mainly influenced by the energy transfer coefficient and the mean free path. The energy transfer coefficient reaches its maximum for a minimum mass difference [31,32]. Considering the atomic masses of the involved elements, Al is much more influenced by collisions with gas particles than the approximately six times heavier Ta atoms, which probably are barely affected. Thus, selective scattering of the lighter Al atoms can be assumed. With increasing p_{O2}, the fraction of the lighter reactive gases present in the chamber also increases, which indicates that selective scattering of Al atoms is the most reasonable explanation for the decreasing Al content with increasing p_{O2}. For TiAlON films a similar behavior was observed, although the decrease of the Al/(Al + Ti) ratio was not that pronounced [13]. However, Ti is considerably lighter than Ta and thus, more affected by collisions with gas elements.

In Fig. 2, the X-ray diffractograms of the TaAl(*O*)N films, from bottom to top with increasing p_{O2} are shown. The standard peak positions for face-centered cubic (fcc) AlN, TaN, TaO (γ-TaO) and wurtzitic (w) AlN are plotted as dashed lines [33–36]. For the TaAlN film deposited without the addition of O, a fcc structure can be observed, with no dominant orientation. Despite the Al/(Al + Ta) ratio of 0.48 of this film, the peaks are quite close to the fcc-TaN standard peak position, but they exhibit a slight shoulder on their right-hand side, suggesting the presence of an additional fcc-AlN-rich phase fraction. In addition, a broad peak at a diffraction angle of ~34° appears, which is attributed to the presence of w-Al(*Ta*)N [37]. Adding $p_{O2} = 0.005$ Pa results in a dominant peak close to the 200 position of fcc-TaN. Compared to the O-free film, the peak is shifted to slightly lower diffraction angles and thus towards the position of fcc-TaO. This is in good agreement with Cristea et al., who investigated sputter deposited TaON films and observed

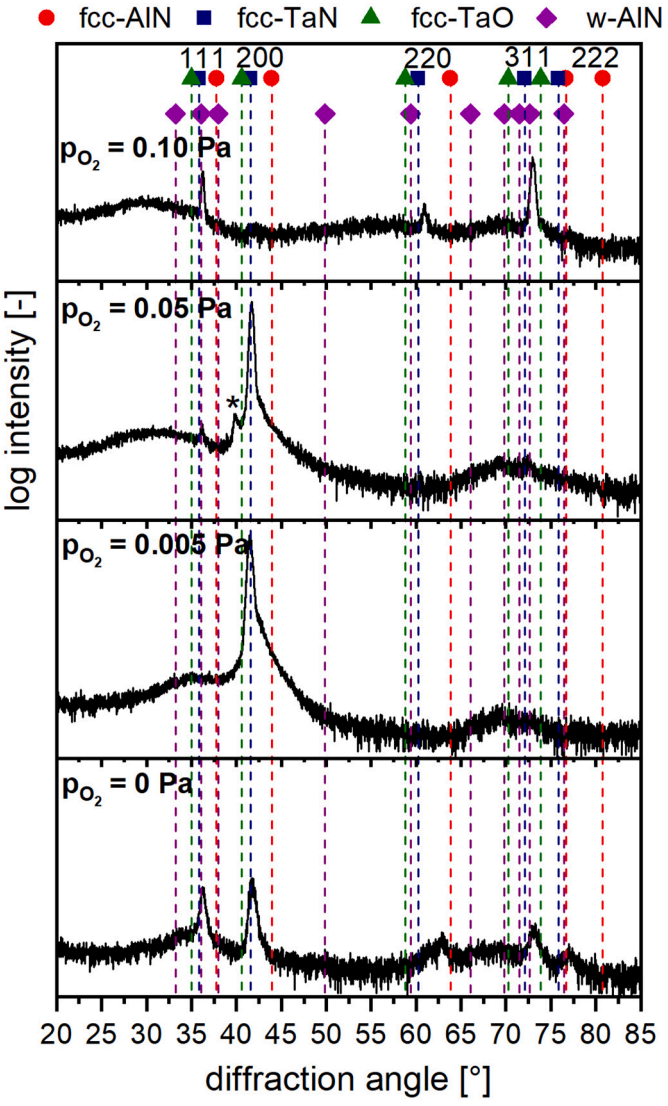

Fig. 2. X-ray diffractogram of the TaAl(*O*)N films from bottom to top with increasing O_2 partial pressure p_{O2}.

peaks between the standard peak positions for fcc-TaN and fcc-TaO [18]. Considering that the film also contains 18 at.% Al, the peak position between fcc-TaO and fcc-AlN indicates the presence of an fcc-$(Ta_{1-x}Al_x)_\delta(O_{1-y}N_y)_\xi$ phase. However, the 200 peak exhibits a pronounced

shoulder on its right-hand side, which can be related to the presence of an fcc-AlN-rich phase fraction. Due to the broad shape of the shoulder a nanocrystalline structure of this fcc-AlN-rich phase fraction can be assumed. Besides the pronounced 200 peak with its shoulder, again a broad peak at a diffraction angle of ~35° appears and another one between 65 and 75°, suggesting the presence of nanocrystalline w-Al(*Ta*)N [37]. Increasing p_{O2} to 0.05 Pa results again in a dominant peak close to the 200 fcc-TaN position, indicating the existence of an fcc-$(Ta_{1-x}Al_x)_\delta(O_{1-y}N_y)_\xi$ phase, with a pronounced shoulder on the right hand side due to an additional fcc-AlN-rich phase fraction. In contrast to the film deposited at $p_{O2} = 0.005$ Pa, the broad peak at ~35° is not visible anymore, but an increased background intensity at low diffraction angles and again between 60 and 80° suggest the presence of an additional amorphous phase fraction. In addition, small peaks are visible, superimposing the increased background intensity. These peaks can be assigned to the 111 and 311 fcc-TaN position. The small peak at ~39.8°, marked with an asterisk, is a measurement artifact due to tube aging ($W_{L\alpha1}$ X-ray emission line). Further increasing of p_{O2} to 0.10 Pa results again in a distinct fcc-structure, but in contrast to the films grown at lower p_{O2} no orientation is dominating and the peaks appear symmetric, missing the shoulder observed in the previous diffractograms due to the fcc-AlN-rich phase fraction. Again the increased background intensity at low diffraction angles is visible, indicating the presence of an additional amorphous phase fraction. For TiAlON and CrAlON films, also an increasing nanocrystalline or amorphous phase fraction with increasing oxygen content has been observed [1,8,11,13,25]. Summarizing, all films up to the highest O content of 26.4 at.% for the film deposited at $p_{O2} = 0.10$ Pa exhibit a dominating fcc-structure, where the random orientation for the O-free film changes to a (100) texture, indicated by the strong 200 peak, when O is added, which is also in good agreement with literature published on TaAlON and CrAlON films with comparable O contents [1,8,11,12,38,39]. Since the (111) plane is the closed packed plane, it is more difficult to accommodate the additional O in (111) oriented crystals compared to (100) oriented ones. Thus, at higher O contents typically the (100) orientation is favored. However, for the present films the texture changes back to random at the highest O content, which can most probably be attributed to the presence of the observed additional amorphous phase fraction, since this phase fraction can also accommodate excess elements.

The film grown at $p_{O2} = 0.05$ Pa was chosen for more detailed investigations using TEM in order to further assess the microstructure and phase composition. In Fig. 3a, a TEM micrograph showing an overview

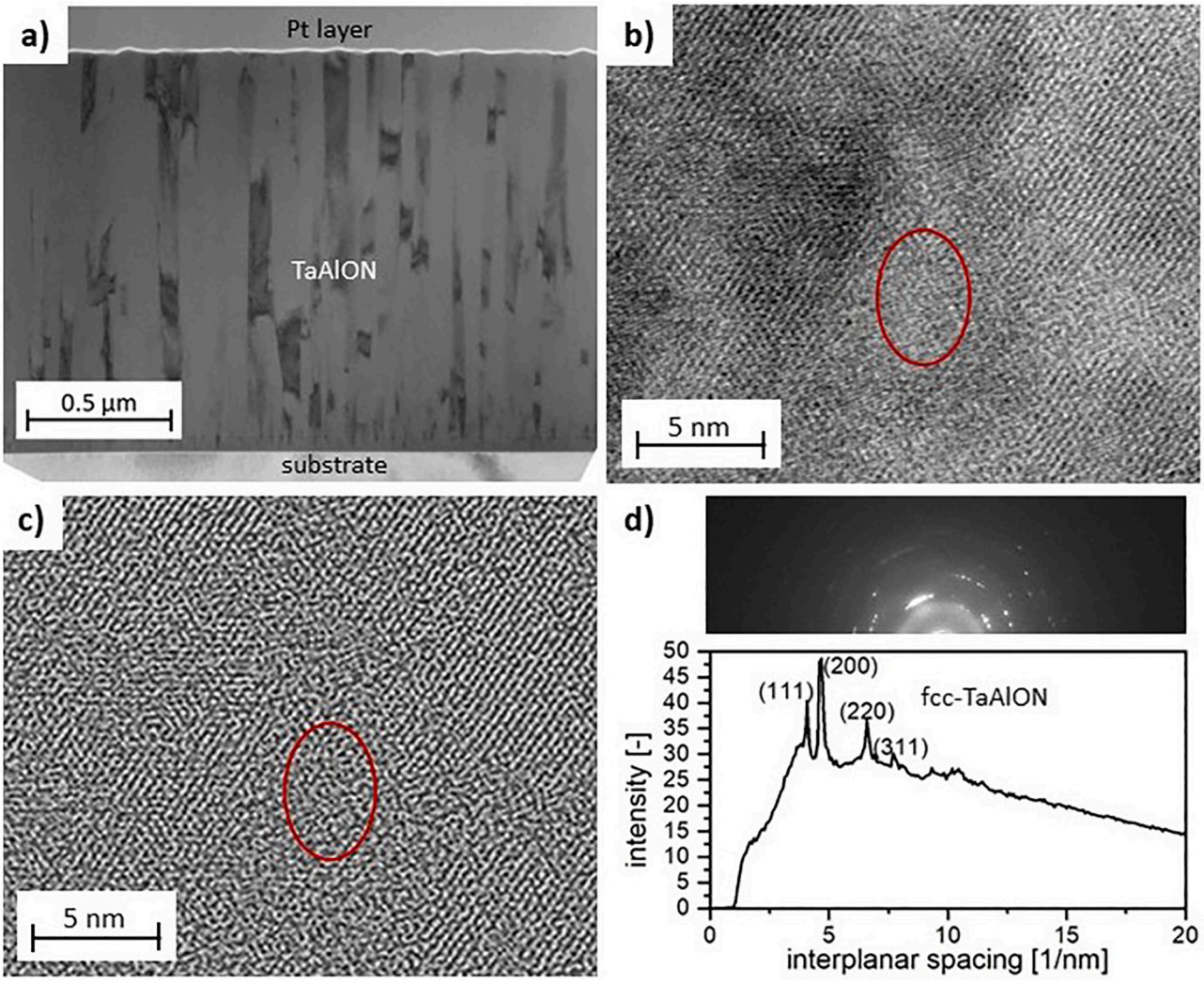

Fig. 3. Transmission electron micrographs showing a) an overview of the TaAlON film and b) a detail captured at high magnification in the middle of the film. In general, the structure appears crystalline, but there are also some disordered regions in-between; one example is marked by the red ellipse. c) Micrograph from b) after image processing (subtraction of a Gaussian-filtered image and application of Fourier filtering) to make the crystalline and disordered regions better visible. d) SAED pattern recorded in the middle of the film and depiction of integrated SAED intensity versus interplanar spacing, exhibiting only reflections of the fcc—$(Ta_{1-x}Al_x)_\delta(O_{1-y}N_y)_\xi$ phase.

of the film is presented. At the substrate/film interface the structure is fine-grained, which is typical for the early stage of competitive grow, followed by a columnar structure. The micrograph in Fig. 3b was taken in the middle of the film with higher magnification. There, clearly a crystalline structure is observed, where even atom rows are visible, but at a closer look there also seem to be disordered regions (marked by the red ellipse). In order to enhance the visibility of the crystalline regions, the background was removed by subtracting a Gaussian-filtered version of the same TEM image and the high frequency noise was removed by applying a Fourier filter. The result is shown in Fig. 3c, where disordered regions interrupting the (nano)crystalline areas can be more clearly distinguished compared to the untreated micrograph. The SAED pattern in Fig. 3d exhibits a bright diffuse ring in the center, indicating the presence of a nanocrystalline/amorphous phase fraction which is in good agreement with the X-ray diffractogram in Fig. 2. The diffraction rings are a bit spotty which results from only a limited number of grains contributing to the SAED pattern due to the columnar structure of the film. To facilitate the identification of the contributing phases, the diffracted intensity has been integrated along the diffraction rings and is displayed over the interplanar spacing in Fig. 3d. There, the reflections are better visible and are in excellent agreement with the standard positions of fcc-TaN and can thus, in accordance to the X-ray diffractogram in Fig. 2, be attributed to the fcc-$(Ta_{1-x}Al_x)_\delta(O_{1-y}N_y)_\xi$ phase. In addition, energy dispersive X-ray spectroscopy (not shown) yielded no evidence for any compositional fluctuations. However, although the TEM lamella was very thin, individual grains might still overlap and blur the result. To obtain locally resolved information about the elemental composition without any overlapping, atom probe tomography would be necessary, which is, however, out of the scope of this work.

In order to obtain information about the chemical bonding states of the films, XPS measurements were conducted. The Ta4f, Al2p, N1s and O1s core level spectra measured at a detection angle of 0° to the surface normal are presented in Fig. 4a–d, respectively, from bottom to top with increasing p_{O2}. The background was subtracted for clearer representation. For the O-free film, the Ta4f spectrum in Fig. 4a can be fitted using three double-peaks, representing contributions (from low to high binding energies) from nitride, O-poor oxynitride and O-rich oxynitride bonds, where the oxynitride bonds stem from surface oxidation after deposition [40,41]. For the three TaAlON films an additional small peak is necessary for a reasonable fit, which is attributed to oxide bonds (most probably Ta_2O_5) [40]. In order to assess which phases are surface contaminates and which phases belong to the "bulk" of the film, all samples were measured under three different detection angles (0, 35 and 50°) to the surface normal (see also Fig. S1 in the Supplementary data). Since the contribution of Ta_2O_5 did not change at different measurement angles, it is assumed that it is a constituent of the actual film. The fact that this phase is not observed in the O-free film further corroborates this assumption. The exact peak positions of the respective contributions are shifted to slightly higher binding energies with increasing p_{O2}, which is related to the changing composition, including a changing Al/(Al + Ta) ratio. However, the peak position of O-rich oxynitride is in good agreement with published values for *in-situ* XPS analysis of TaON layers [41]. The Al2p core level spectra in Fig. 4b exhibit one broad peak, comprising nitride, oxynitride and oxide contributions [22]. With increasing p_{O2}, the peak is slightly shifted to higher binding energies, indicating an increasing amount of oxide bonds in the film [1]. Further, it seems that the intensity of the peak decreases with increasing p_{O2}, which is in good agreement with the observed decrease of the Al content. At binding energies between ~70 and 72 eV, one (for the TaAlN film) or two (for the O-containing films) additional small peaks are visible, which are related to the Ta5s orbital [42]. In Fig. 4c the N1s core level spectra are shown with a distinct peak at binding energies of ~396 eV, which is mainly due to oxynitride bonds, but also contains a contribution of nitride bonds [43]. The intensity of the oxynitride peak seems to slightly decrease with increasing p_{O2}, which is in good agreement with the slightly decreasing N content. At higher binding energies, two additional broad peaks are present which are related to the $Ta4p_{3/2}$ orbital [40]. The O1s orbital in Fig. 4d can be fitted using three peaks. While the peak at the lowest binding energy comprises contributions of oxide and O-rich oxynitride bonds and the second peak stems from O-poor oxynitride bonds, the one at a binding energy of 532 eV is related to surface contaminations (hydroxylation), as corroborated by an additional XPS measurement without breaking the vacuum after a vacuum annealing treatment, where this peak vanished [44]. The spectrum of the O-free films does not significantly differ from the ones of the O-containing films. However, in contrast to the O-containing films, the spectrum of the O-free film varies at different measurement angles, strongly indicating that mainly surface oxidation of the TaAlN is responsible for the observed bonds, which is also in agreement with the detected O content of <1 at.% (Fig. 1a) in this film.

In Fig. 5, the results of the complementarily performed Raman spectroscopy measurements are shown. Typical positions for TaN and Ta_2O_5 bands reported in literature are added as dashed lines [45,46]. In excellent agreement with the XPS study, no evidence for Ta_2O_5 can be observed for the O-free film, which exhibits the typical spectrum for TaN [45], while additional bands appear for the O-containing films, indicating the presence of Ta_2O_5 [46,47]. Since no crystalline Ta_2O_5 could be detected using XRD, it can be assumed that it exists in an amorphous structure.

In Fig. 6, the evolution of the hardness and elastic modulus of the TaAl(*O*)N films are shown as a function of p_{O2}. In general, a trend to lower hardness values with increasing p_{O2} can be observed, analogously to literature on TiAlON, where a similarly decreasing hardness with increasing O content due to an increasing amorphous phase fraction has been reported [1,13,25]. The elastic modulus likewise decreases with increasing O content, which has also been observed for TiAlON and was attributed to the formation of metal vacancies and comparably weak metal-oxygen bonds [12,25]. The TaAlN film deposited without O exhibits unexpectedly low hardness and elastic modulus values. An evaluation of the strain of the films using XRD revealed that the O-free film exhibits tensile strain, indicating a tensile stress state, while all O-containing films show compressive strain, indicating a compressive stress state. Due to the unfavorable X-ray diffractograms and peak shapes for stress determination and the unknown X-ray elastic constants for TaAlON no stress values were determined and only the magnitude was considered. However, in addition to the w-phase fraction observed in XRD for the O-free film, tensile stress is a plausible explanation for the comparably low hardness and elastic modulus of the TaAlN film.

4. Conclusion

A series of TaAl(*O*)N thin films was deposited by unbalanced d.c. magnetron sputter deposition applying constant nitrogen and increasing oxygen partial pressure, resulting in oxygen contents between 0 and 26 at.%. In addition to a decreasing metal/non-metal ratio, as also commonly observed for TiAlON, the increasing oxygen content was accompanied by a significantly decreasing Al/(Al + Ta) ratio which was attributed to selective scattering of light Al atoms. For all films a dominating fcc-structure was observed, which changed from randomly oriented for the oxygen-free film to (200) oriented with the addition of oxygen and back to random at the highest oxygen content. It was assumed that the changing texture is affected by the additionally observed nanocrystalline and amorphous phase fractions present in the oxygen containing films. X-ray photoelectron and Raman spectroscopy consistently revealed the presence of Ta_2O_5 in the oxide containing films, which is most probably amorphous, since no evidence for crystalline Ta_2O_5 could be detected using X-ray diffraction. The hardness and elastic modulus of the films decreased with increasing oxygen content, due to the increasing amorphous phase fraction and the formation of metal vacancies and weak metal-oxygen bonds, respectively. Considering that in contrast to the transition metals (TM) typically used in literature for the synthesis of TMAlON, the oxide of Ta (Ta_2O_5)

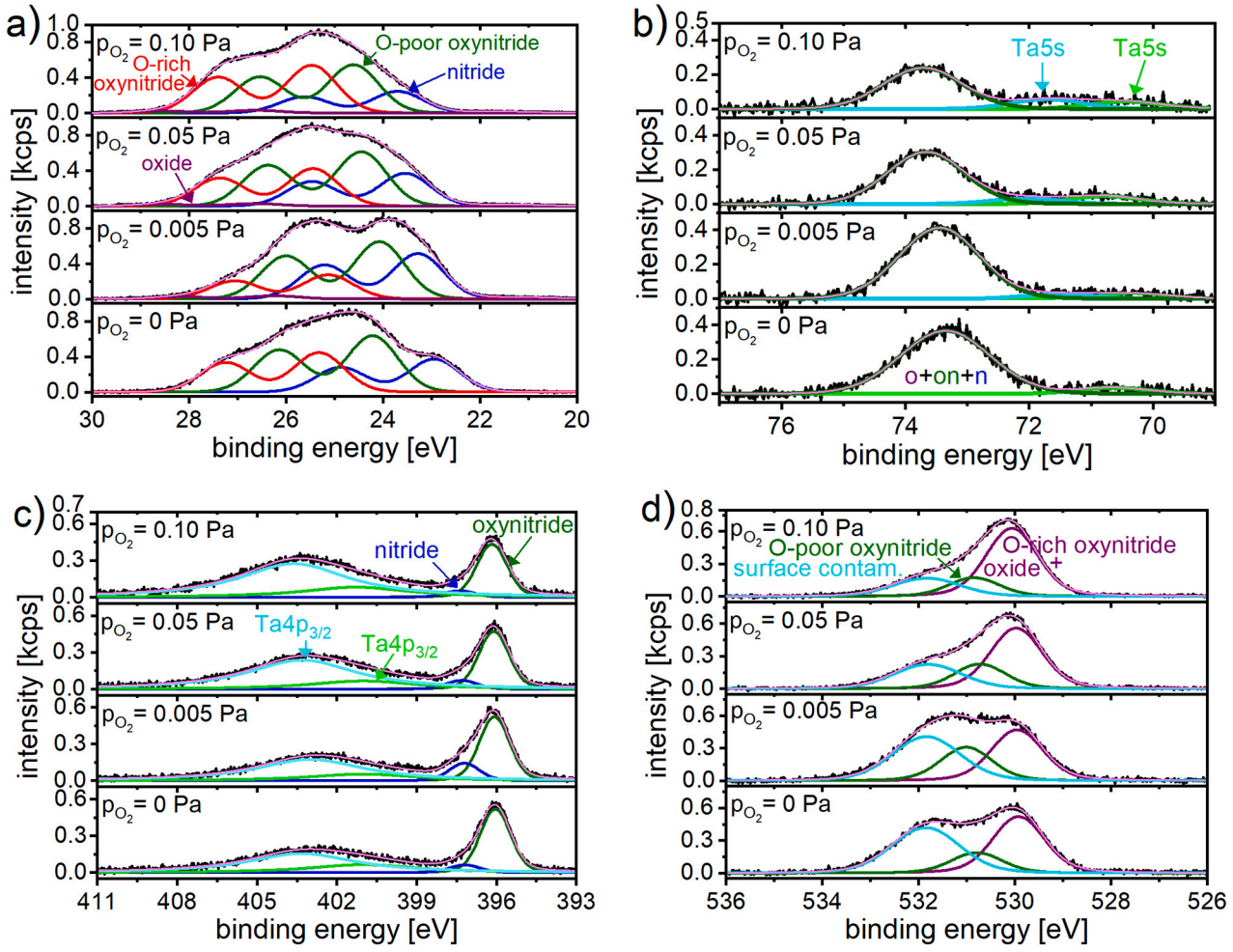

Fig. 4. Summary of the (a) Ta4f, (b) Al2p, (c) N1s and (d) O1s core level spectra of TaAl(*O*)N films deposited from bottom to top with increasing O_2 partial pressure p_{O2}, determined by XPS.

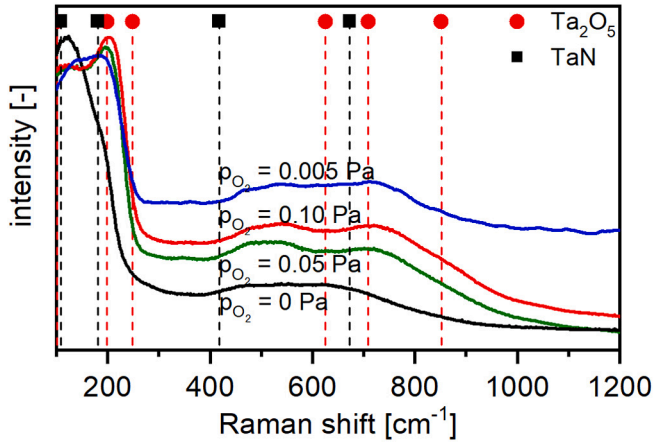

Fig. 5. Raman signal of TaAl(*O*)N films deposited at different O_2 partial pressure p_{O2}.

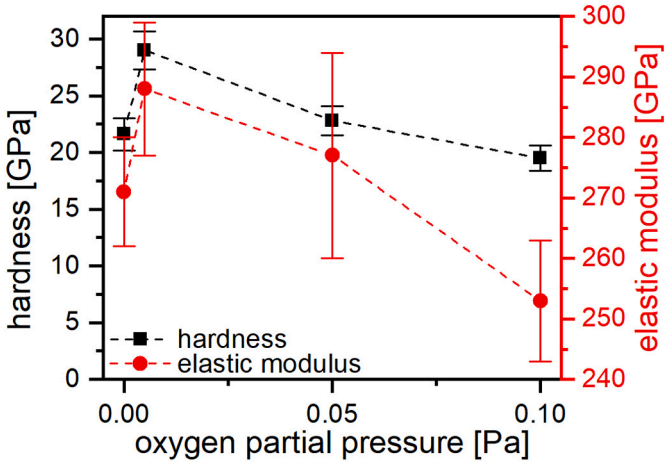

Fig. 6. Hardness and elastic modulus of the TaAl(*O*)N films as a function of the O_2 partial pressure p_{O2}.

exhibits a more negative enthalpy of formation compared to Al, this work provides the basis to establish a fundamental understanding of the phase formation in TMAlON depending on the involved elements. For a more detailed evaluation of the present phases and in particular their compositions, complementary application of high resolution methods with special focus on atom probe tomography investigations will be necessary in the future.

Supplementary data to this article can be found online at https://doi.org/10.1016/j.surfcoat.2021.127237.

CRediT authorship contribution statement

Nina Schalk: Conceptualization, Methodology, Validation, Formal analysis, Writing – original draft, Visualization, Project administration, Funding acquisition. **Christian Saringer:** Methodology, Investigation, Validation, Writing – review & editing. **Alexander Fian:** Methodology, Investigation, Validation, Writing – review & editing. **Velislava L. Terziyska:** Methodology, Investigation. **Jaakko Julin:** Methodology, Investigation, Validation, Writing – review & editing. **Michael Tkadletz:** Methodology, Validation, Writing – review & editing.

Declaration of competing interest

The authors declare that they have no known competing financial interests or personal relationships that could have appeared to influence the work reported in this paper.

Acknowledgements

The authors are grateful to Dr. Ilse Letofsky-Papst (Institute of Electron Microscopy and Nanoanalysis (FELMI), Graz University of Technology) for the TEM investigations. Funding for this research has been provided by the Austrian Federal Ministry for Digital and Economic Affairs and the National Foundation for Research, Technology and Development (grant number CDL-ACCT).

References

[1] J. Sjölen, L. Karlsson, S. Braun, R. Murdey, A. Hörling, L. Hultman, Structure and mechanical properties of arc evaporated Ti-Al-O-N thin films, Surf. Coat. Technol. 201 (2007) 6392–6403.
[2] K. Tönshoff, B. Karpuschewski, A. Mohlfeld, T. Leyendecker, G. Erkens, H.G. Fuß, R. Wenke, Performance of oxygen-rich TiAlON coatings in dry cutting applications, Surf. Coat. Technol. 108–109 (1998) 535–542.
[3] L. Rebouta, A. Pitães, M. Andritschky, P. Capela, M.F. Cerqueira, A. Matilainen, K. Pischow, Optical characterization of TiAlN/TiAlON/SiO_2 absorber for solar selective applications, Surf. Coat. Technol. 211 (2012) 41–44.
[4] N. Selvakumar, H.C. Barshilia, Review of physical vapor deposited (PVD) spectrally selective coatings for mid- and high-temperature solar thermal applications, Sol. Energy Mater. Sol. Cells 98 (2012) 1–23.
[5] H.C. Barshilia, Growth, characterization and performance evaluation of Ti/AlTiN/AlTiON/AlTiO high temperature spectrally selective coatings for solar thermal power applications, Sol. Energy Mater. Sol. Cells 130 (2014) 322–330.
[6] K. Kawata, H. Sugimura, O. Takai, Characterization of multilayer films of Ti-Al-O-C-N system prepared by pulsed d.c. plasma-enhanced chemical vapor deposition, Thin Solid Films 390 (2001) 64–69.
[7] M. Stueber, D. Diechle, H. Leiste, S. Ulrich, Synthesis of Al–Cr–O–N thin films in corundum and f.c.c. structure by reactive r.f. magnetron sputtering, Thin Solid Films 519 (2011) 4025–4031.
[8] H. Najafi, A. Karimi, E. Oveisi, M. Morstein, Structure and electronic properties of $AlCrO_xN_{1-x}$ thin films deposited by reactive magnetron sputtering, Thin Solid Films 572 (2014) 176–183.
[9] A. Khatibi, J. Sjölen, G. Greczynski, J. Jensen, P. Eklund, L. Hultman, Structural and mechanical properties of Cr-Al-O-N thin films grown by cathodic arc deposition, Acta Mater. 60 (2012) 6494–6507.
[10] A. Khatibi, A. Genvad, E. Göthelid, J. Jensen, P. Eklund, L. Hultman, Structural and mechanical properties of corundum and cubic $(Al_xCr_{1-x})_{2+y}O_{3-y}$ coatings grown by reactive cathodic arc evaporation in as-deposited and annealed states, Acta Mater. 61 (2013) 4811–4822.
[11] C. Gnoth, C. Kunze, M. Hans, M. to Baben, J. Emmerlich, J.M. Schneider, G. Grundmeier, Surface chemistry of TiAlN and TiAlNO coatings deposited by means of high power pulsed magnetron sputtering, J. Phys. D. Appl. Phys. 46 (2013) 084003.
[12] M. Hans, M. to Baben, D. Music, J. Ebenhöch, D. Primetzhofer, D. Kurapov, M. Arndt, H. Rudigier, J.M. Schneider, Effect of oxygen incorporation on the structure and elasticity of Ti-Al-O-N coatings synthesized by cathodic arc and high power pulsed magnetron sputtering, J. Appl. Phys. 116 (2014) 093515.
[13] N. Schalk, M. Tkadletz, V.L. Terziyska, M. Deluca, I. Letofsky-Papst, J. Keckes, C. Mitterer, Evolution of microstructure and mechanical properties of a graded TiAlON thin film investigated by cross-sectional characterization techniques, Surf. Coat. Technol. 359 (2019) 155–161.
[14] M. Stüber, U. Albers, H. Leiste, K. Seemann, C. Ziebert, S. Ulrich, Magnetron sputtering of hard Cr–Al–N–O thin films, Surf. Coat. Technol. 203 (2008) 661–665.
[15] I.A. Khan, M. Hassan, T. Hussain, R. Ahmad, M. Zakaullah, R.S. Rawat, Synthesis of nano-crystalline zirconium aluminium oxynitride (ZrAlON) composite films by dense plasma focus device, Appl. Surf. Sci. 255 (2009) 6132–6140.
[16] J. Zhu, Z.G. Liu, Y.R. Li, HfAlON films fabricated by pulsed laser ablation for high-k gate dielectric applications, Mater. Lett. 59 (2005) 821–825.
[17] NIST chemistry webbook, NIST Standard Reference Database Number 69. Http://Webbook.Nist.Gov/Chemistry/.
[18] D. Cristea, D. Constantin, A. Crisan, C.S. Abreu, J.R. Gomes, N.P. Barradas, E. Alves, C. Moura, F. Vaz, L. Cunha, Properties of tantalum oxynitride thin films produced by magnetron sputtering: the influence of processing parameters, Vacuum. 98 (2013) 63–69.
[19] M. Hans, M. to Baben, Y.-T. Chen, K.G. Pradeep, D.M. Holzapfel, D. Primetzhofer, D. Kurapov, J. Ramm, M. Arndt, H. Rudigier, J.M. Schneider, Substrate rotation-induced chemical modulation in Ti-Al-O-N coatings synthesized by cathodic arc in an industrial deposition plant, Surf. Coat. Technol. 305 (2016) 249–253.
[20] NIST, X-ray photoelectron spectroscopy database. https://srdata.nist.gov/xps/.
[21] G. Greczynski, L. Hultman, X-ray photoelectron spectroscopy: towards reliable binding energy referencing, Prog. Mater. Sci. 107 (2020) 100591.
[22] J.F. Moulder, W.F. Stickle, P.E. Sobol, K.D. Bomben, Handbook of X-ray Photoelectron Spectroscopy, Pysical Electronics, Inc., Eden Prairie, 1995.
[23] S. Hofmann, Auger-and X-ray Photoelectron Spectroscopy in Materials Science: A User-oriented Guide, Springer, Berlin, 2013.
[24] D.A. Shirley, High-resolution X-ray photoemission spectrum of the valence bands of gold, Phys. Rev. B 5 (1972) 4709.
[25] N. Schalk, J.F.T.S. Fotso, D. Holec, A. Fian, G. Jakopic, V.L. Terziyska, R. Daniel, C. Mitterer, Microstructure, mechanical and optical properties of TiAlON coatings sputter-deposited with varying oxygen partial pressures, J. Phys. D. Appl. Phys. 49 (2016) 25307.
[26] H. Najafi, A. Karimi, M. Morstein, Microstructure of $Al_{95.5}Cr_{2.5}Si_2(N_{1-x}O_x)$ thin films covering from nitrides to oxides, Surf. Coat. Technol. 205 (2011) 5199–5204.
[27] D. Depla, A. Colpaert, K. Eufinger, A. Segers, J. Haemers, R. De Gryse, Target voltage behaviour during DC sputtering of silicon in an argon/nitrogen mixture, Vacuum. 66 (2002) 9–17.
[28] D. Depla, R. De Gryse, Target poisoning during reactive magnetron sputtering: part I: the influence of ion implantation, Surf. Coat. Technol. 183 (2004) 184–189.
[29] D. Depla, R. De Gryse, Target poisoning during reactive magnetron sputtering: part III: the prediction of the critical reactive gas mole fraction, Surf. Coat. Technol. 183 (2004) 196–203.
[30] J.F. Ziegler, M.D. Ziegler, J.P. Biersack, SRIM - The Stopping and Range of Ions in Matter, Version SRIM. www.SRIM.org, 2013.
[31] M. Konuma, Film Deposition by Plasma Techniques, Springer, Berlin, 1992.
[32] C. Mitterer, P.H. Mayrhofer, E. Kelesoglu, R. Wiedemann, H. Oettel, Internal growth parameters - a suitable basis for comparison of PVD coatings, Z. Metallkd. 90 (1999) 602–607.
[33] Int. Cent. Diffr. Data, Pdf-2/Release, 2007 card number 00-025-1495.
[34] Int. Cent. Diffr. Data, Pdf-2/Release, 2007 card number 00-049-1283.
[35] Int. Cent. Diffr. Data, Pdf-2/Release, 2007 card number 01-072-2740.
[36] Int. Cent. Diffr. Data, Pdf-2/Release, 2007 card number 01-076-0702.
[37] B. Grossmann, N. Schalk, C. Czettl, M. Pohler, C. Mitterer, Phase composition and thermal stability of arc evaporated $Ti_{1-x}Al_xN$ hard coatings with $0.4 \leq x \leq 0.67$, Surf. Coat. Technol. 309 (2017) 687–693.
[38] Y. Liu, Y. Dong, W. Zhao, G. Li, Microstructure and mechanical properties of (Al,Ti)(O,N) coatings prepared by reactive sputtering, Int. J. Refract. Met. Hard Mater. 25 (2007) 271–274.
[39] F. Mei, Y. Dong, Y. Li, G. Li, Microstructure and mechanical properties of (Ti,Al)(O,N) films synthesized by reactive sputtering, Mater. Lett. 60 (2006) 375–378.
[40] D. Cristea, L. Cunha, C. Gabor, I. Ghiuta, C. Croitoru, A. Marin, L. Velicu, A. Besleaga, B. Vasile, Tantalum oxynitride thin films: assessment of the photocatalytic efficiency and antimicrobial capacity, Nanomat. 9 (2019) 476.
[41] J. Tao, J.W. Chai, L.M. Wong, Z. Zhang, J.S. Pan, S.J. Wang, Growth of single crystalline TaON on yttria-stabilized zirconia (YSZ), J. Solid State Chem. 204 (2013) 27–31.
[42] R. Nyholm, A. Berndtsson, N. Martensson, Core level binding energies for the elements Hf to Bi (Z=72-83), J. Phys. C Solid State Phys. 13 (1980) L1091.
[43] P. Lamour, P. Fioux, A. Ponche, M. Nardin, M.F. Vallat, P. Dugay, J.P. Brun, N. Moreaud, J.M. Pinvidic, Direct measurement of the nitrogen content by XPS in self-passivated TaN_x thin films, Surf. Interface Anal. 40 (2008) 1430–1437.
[44] Y. Tanaka, M. Nakai, T. Akahori, M. Niinomi, Y. Tsutsumi, H. Doi, T. Hanawa, Characterization of air-formed surface oxide film on Ti-29Nb-13Ta-4.6Zr alloy surface using XPS and AES, Corros. Sci. 50 (2008) 2111–2116.
[45] G.B. Gaitán, A. Milena, E. García, A. Caterine, Q. Ossa, J. Alberto, O. Vélez, Deposition and property characterisation of TaN coatings with different nitrogen contents, Rev. EIA 13 (2016) 69–80.
[46] A.C. Cefalas, Z. Kollia, N. Spyropoulos-Antonakakis, V. Gavriil, D. Christofilos, G. Kourouklis, V.V. Semashko, V. Pavlov, E. Sarantopoulou, Surface profile gradient in amorphous Ta_2O_5 semi conductive layers regulates nanoscale electric current stability, Appl. Surf. Sci. 396 (2017) 1000–1019.
[47] E. Mendoza-Mendoza, A.G. Nuñez-Briones, R. Leyva-Ramos, R.D. Peralta-Rodríguez, L.A. García-Cerda, E.D. Barriga-Castro, R. Ocampo-Pérez, J. Rodríguez-Hernández, A novel two-step route for synthesizing pure Ta_2O_5 nanoparticles with enhanced photocatalytic activity, Ceram. Int. 45 (2019) 6268–6274.